Progress In Electromagnetics Research, Vol. 184, 32–42, 2025

(Received 28 August 2025, Accepted 27 November 2025, Scheduled 11 December 2025)

Magneto-Optical Driven Topological Polarization Singularities Modulation in the Photonic Crystal Slab

Bo Yang[1, 2], Wanhua Zheng[2, 3, 4, *], and Anjin Liu[1, 2, 4, *]

[1] *State Key Laboratory of Optoelectronic Materials and Devices*
Institute of Semiconductors, Chinese Academy of Sciences, Beijing 100083, China
[2] *Center of Materials Science and Optoelectronics Engineering*
University of Chinese Academy of Sciences, Beijing 100049, China
[3] *Key Laboratory of Solid-State Optoelectronics Information Technology*
Institute of Semiconductors, Chinese Academy of Sciences, Beijing 100083, China
[4] *Hangzhou Institute for Advanced Study, University of Chinese Academy of Sciences, Hangzhou 310024, China*

ABSTRACT: The modulation of topological polarization singularities in momentum space in photonics has attracted much attention due to their relations with bound states in the continuum (BICs), unidirectional guided resonances, and chirality. Current modulation strategies that rely on structural symmetry breaking or phase-change materials are challenging to achieve dynamic and flexible modulation of polarization singularities. Recently, magneto-optical (MO) modulation of light provides a promising theoretical strategy for the dynamic modulation of polarization singularities. However, the dynamics of transverse electric (TE)/transverse magnetic (TM)-mode singularities under varying magnetic fields remain elusive in the MO photonic crystal (PhC) slab. Herein, we systematically investigate the dynamic modulation of topological polarization singularities in the PhC slabs with square arrays of square air holes and deformed square air holes based on the MO effect. In-plane (x/y) magnetic fields have no effect on the TE mode of the MO PhC slab. However, the fields induce splitting and separation of vortex polarization singularity (V point) of the TM mode into a pair of circular polarization points (C points), enabling extrinsic chirality without breaking the structural symmetry. A magnetic field along the z direction enables near-unity circular dichroisms (CDs) over a broad angular range when circular polarizations are formed at off-Γ points for the TE and TM modes. Furthermore, by introducing single symmetry breaking (in-plane symmetry breaking for TE, out-of-plane symmetry breaking for TM) with magnetic field tuning, one of the C points can be shifted to the Γ point, resulting in intrinsic chiral quasi-BICs (QBICs) with ultrahigh Q-factors and near-unity CDs. This study provides a dynamic and flexible modulation approach for polarization singularities, which enhances light-matter interactions for applications in advanced chiral photonic devices and tunable optoelectronic devices.

1. INTRODUCTION

A singularity refers to a special point where physical quantities exhibit singularity or are undefined. In the field of optics, singularities can be classified into intensity, phase, and polarization singularities based on different levels of light description [1–3]. Among them, topological polarization singularities in momentum space have attracted much attention due to their close connection with topological phenomena such as bound states in the continuum (BICs), unidirectional guided resonances (UGRs), and chirality [4–12]. These singularities play a crucial role in enhancing light-matter interactions and in the field of topological photonics [13–17].

These singularities are categorized into three types: vortex polarization singularities (V points) carrying integer topological charges, circular polarization points (C points) carrying half-integer charges, and lines where the polarization is linear (L lines) [7]. In lossless infinite structures or in structures with infinite or zero permittivity, V points usually correspond to ideal BICs with infinite quality factors (Q-factors) [18, 19]. It has been proven that BIC is the vortex center characterized by polarization vectors [20, 21]. Different from V points, the eigenmodes at C points have finite Q factors and only couple with circularly polarized light of a specific chirality, directly causing chiroptical effects [6, 16, 22–24]. The topological properties of these singularities provide a theoretical basis for the design of applications such as directional radiation devices, ultrahigh-Q guided resonances, and optical vortex lasers [25–30].

Current approaches for manipulating topological polarization singularities mainly rely on structural symmetry breaking or phase-change materials. Breaking the in-plane C_2 symmetry of the structures allows the V point to be decomposed into a pair of C points [31]. Recently, several flexible mechanisms have been proposed to generate and tune C points [7, 31, 32]. For example, the generation, merging, and annihilation of pairs of C points in two misaligned stacked dielectric gratings are constrained by the conservation of global topological charge [7]. Similarly, breaking mirror symmetry enables tilted gratings to transform accidental BICs into UGRs, accompanied by the separation and merging of V points [8, 12]. However, the evolution trajectories of singularities are strictly constrained by designed structural parameters, making dynamic modulation of

---

* Corresponding authors: Wanhua Zheng (whzheng@semi.ac.cn); Anjin Liu (liuanjin@semi.ac.cn).

doi:10.2528/PIER25082804

Published by THE ELECTROMAGNETIC ACADEMY

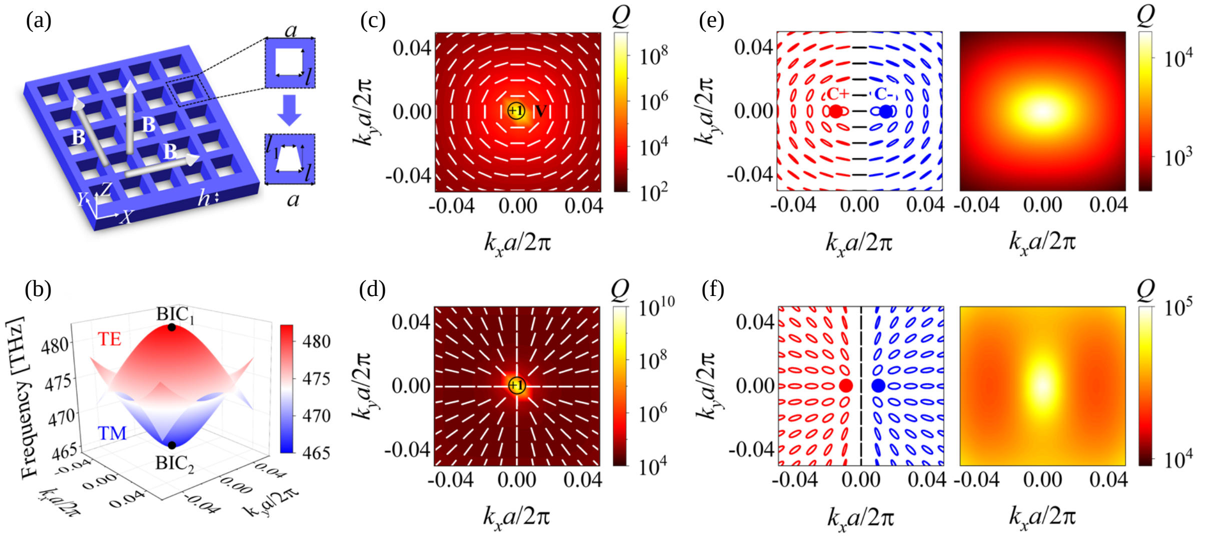

FIGURE 1. (a) Schematic of the MO PhC slab, with the insets showing the unit cell with C_{4v} symmetry (top) and C_2 symmetry breaking (bottom). (b) Band structures of the MO PhC slab without structural perturbation, where the Γ points of the TE-like and TM-like bands are both BICs. Far-field polarization states of the (c) TE and (d) TM bands with C_{4v} symmetry, with the background color representing the magnitude of the Q-factor. Far-field polarization states and Q-factors of the (e) TE and (f) TM bands with C_2 symmetry breaking. The white lines represent the intrinsic linear polarization states, and the red (blue) ellipses represent right- (left-) handed polarization states. The red (blue) dots represent RCP and LCP states, corresponding to C+ and C− points, respectively.

singularity trajectories challenging. On the other hand, modulation strategies based on phase-change materials like Sb_2Se_3 are constrained by the intrinsic phase-change dynamics of these materials [33]. The existing passive modulation mechanisms are inadequate for achieving real-time and dynamic manipulation of polarization singularities. It is very necessary to propose new dynamic modulation strategies.

Recently, the magneto-optical (MO) modulation has emerged as a novel approach for dynamically manipulating polarization singularities [34–39]. Applying a magnetic field to an MO photonic crystal (PhC) slab can enable the robust generation of intrinsic C points as MO BICs [35]. This approach can also achieve the modulation of arbitrary polarizations of the transverse electric (TE) mode around the BIC and intrinsic chirality at the Γ point [36]. MO modulation can break the in-plane C_2 symmetry while preserving inversion spatial symmetry in an MO grating, resulting in the splitting of the V point into a pair of C points [37]. The movement of C points in momentum space can be controlled by adjusting the magnetic field strength. Additionally, MO modulation can induce the splitting of degenerate BICs, resulting in spin-orbit-locking chiral BICs in the MO PhC slab [38]. The MO modulation has demonstrated remarkable advantages. However, for practical applications enabled by V points and C points in momentum space, the dynamics of singularities in TE and transverse magnetic (TM) modes in the MO PhC slab under magnetic fields of varying directions and magnitudes remain elusive.

In this work, we investigate the dynamic modulation of topological polarization singularities in the MO PhC slabs with square arrays of square air holes (C_2 symmetry protection) and deformed square air holes (symmetry breaking). The modulation is studied under magnetic fields with different directions and strengths. Under the C_2 symmetry of the MO PhC slab, in-plane (x/y) magnetic fields lead to the far-field polarization states of the TE mode unchanged, but introduce extrinsic chirality in TM mode by splitting the V point into two C points that separate with increasing field strength. Control over arbitrary polarization states at off-Γ points in both TE and TM modes can be achieved under the z direction magnetic field, rather than being limited to the TE mode alone. The circular polarization states at off-Γ points can enable near-unity circular dichroisms (CDs) over a broad angular range in TE and TM modes. By introducing symmetry breaking of the MO PhC slab (in-plane symmetry breaking for TE, out-of-plane symmetry breaking for TM) with magnetic tuning one of the C points can be shifted to the Γ point, thereby realizing intrinsic chiral quasi-BICs (QBICs) with ultra-high Q-factors and near-unity CDs. This study provides a flexible strategy to effectively manipulate V and C points, and is useful for applications of topological photonics in enhancing light-matter interactions.

2. STRUCTURE AND MODEL

Figure 1(a) shows a schematic of a two-dimensional PhC slab composed of MO materials. The unit cell of the MO PhC slab is with C_{4v} symmetry, featuring a period $a = 400\,\text{nm}$, a thickness $h = 370\,\text{nm}$, and a square air hole width $l = 280\,\text{nm}$. In our calculations, the finite element method is employed. Periodic boundary conditions are applied in the x and y directions, and perfectly matched layers are set in the z direction. The finite thickness of the PhC slab results in the absence of pure TE and TM modes. Therefore, the modes mentioned in this paper are TE-like and TM-like modes. As shown in Fig. 1(b), the TE-like and TM-like band structures in momentum space are calculated. Two symmetry-protected BICs (SP-BICs) carrying integer topological charges can be identified at the Γ points of the TE and TM bands, denoted as BIC_1 and BIC_2, respectively.

BIC is the vortex center of the far-field radiation polarization, carrying an integer topological charge. The topological charge describes the winding number of the polarization vector around the polarization singularity and is defined as [5]

$$q = \frac{1}{2\pi} \oint_L d\mathbf{k} \cdot \nabla_k \phi(\mathbf{k}), \tag{1}$$

where $\phi(\mathbf{k})$ represents the orientation angle between the long axis of polarization and the x-axis, and L is a closed loop rotating counterclockwise around the polarization singularity in momentum space. When the polarization vector cannot be continuously defined, a non-zero topological charge emerges, resulting in the formation of polarization singularities [7]. Topological singularities correspond to combinations of Stokes parameters. The V point carries an integer topological charge, where $S_1 = S_2 = S_3 = 0$ [40, 41], whereas the C point carries a half-integer topological charge with $S_1 = S_2 = 0$ and $S_3 = \pm 1$ [6]. To confirm the existence of SP-BICs, we calculate the distributions of the far-field polarization states and Q-factors around the Γ points for the TE and TM modes, as shown in Figs. 1(c) and (d). The far-field polarization vectors form vortices, and the ultra-high Q-factors at the Γ points confirm the existence of two BICs. The distributions of the polarization vectors around the BIC$_1$ and BIC$_2$ are given by $\phi(\mathbf{k}) \propto k_y - ik_x$ and $\phi(\mathbf{k}) \propto k_x + ik_y$ [15], respectively. From Eq. (1), the topological charge carried by the BICs is $+1$.

Additionally, in order to convert BIC to QBIC, a geometric perturbation $\Delta l = l - l_1$ is introduced, which can break the in-plane C_2 symmetry of the MO PhC slab. As shown in Fig. 1(a), the squares are transformed into isosceles trapezoids, where l1 denotes the upper base of each trapezoid. Here, we set $l_1 = 260$ nm ($\Delta l = 20$ nm). As shown in Figs. 1(e) and (f), the V point splits into a pair of C points. Each C point has a topological charge of 1/2, symmetrically distributed on the two sides of the Γ point. The C+ and C− points correspond to left-handed circular polarization (LCP) and right-handed circular polarization (RCP) states, respectively. For TE and TM modes, the C points are located at $(k_x a/2\pi, k_y a/2\pi) = (\pm 0.012, 0)$ and $(k_x a/2\pi, k_y a/2\pi) = (\pm 0.008, 0)$, respectively.

3. RESULTS AND DISCUSSIONS

When an external magnetic field is applied to the MO PhC slab, the time-reversal symmetry (TRS) of the system is broken. The magnetic field induces spin-orbit-coupling within the material, and introduces off-diagonal elements into the permittivity tensor of the MO material. The external magnetic field results in the emergence of optical anisotropy of the MO PhC slab. Up to the first order of magnetization, symmetry arguments and Onsager's relations indicate that for the permittivity $\varepsilon_{ij}(B)$ $(i \neq j)$, each pair of symmetric components is proportional to the ± components of magnetic field induction B [42]. For MO materials, the magnetic linear birefringence is generally very weak. The Cotton-Mouton effect is not considered in the permittivity tensor. Therefore, under an external magnetic field, the optical response of the MO PhC slab takes the following relative permittivity tensor [42, 43]:

$$\overleftrightarrow{\varepsilon} = \begin{bmatrix} \varepsilon & -i\delta_z & -i\delta_y \\ i\delta_z & \varepsilon & -i\delta_x \\ i\delta_y & i\delta_x & \varepsilon \end{bmatrix}, \tag{2}$$

where ε in the diagonal elements is the dielectric constant and set to 5 in the spectral region of interest in our calculations [39, 44]. By adjusting the bismuth doping concentration, this value falls within the permittivity range of bismuth-doped yttrium iron garnet (Bi : YIG) [44]. The off-diagonal elements δ_x, δ_y, and δ_z are the components of the Voight vector, which describe the results induced by magnetic fields applied along the x, y, and z directions, respectively. Their magnitudes are proportional to strength of the external magnetic field induction B. The MO PhC slab will be placed in an electromagnetic coil, which can provide the required external magnetic field for the slab. Experimental results have shown that when a feasible magnetic field ($B \approx 1$ T) is applied, the magnitudes $|\delta_x|$, $|\delta_y|$, and $|\delta_z|$ for the off-diagonal elements of the permittivity tensor can reach 0.5 [11, 44]. The all-dielectric MO materials exhibit low optical absorption at visible wavelengths and lossless optical response at the infrared range [45]. Therefore, the intrinsic dispersion and absorption losses of the MO material are neglected for the theoretical prediction. The MO material used here can be practically realized by employing low-loss MO materials, such as cerium-doped YIG (Ce : YIG) [46], Bi : YIG [44, 45], and bismuth-iron-garnet (BIG) [47].

When a magnetic field is applied in the z direction, $\delta_x = \delta_y = 0$ and $\delta_z \neq 0$. Negative δ_x, δ_y, and δ_z represent the applied magnetic field directions along the $-x$, $-y$, and $-z$ directions, respectively. When $\delta \neq 0$, $\vec{\varepsilon}^* \neq \vec{\varepsilon}$, the TRS is broken. The wave equation of the MO PhC slab can be expressed as [48, 49]

$$\nabla \times \mu_r^{-1} (\nabla \times \mathbf{E}) - k_0^2 \left(\overleftrightarrow{\varepsilon} - \frac{j\sigma}{\omega \varepsilon_0} \right) \mathbf{E} = 0, \tag{3}$$

where σ represents the electrical conductivity, μ_r the relative magnetic permeability, $\mathbf{E}$ the electric field vector, k_0 the wavevector in free space, ω the frequency, and j represents the imaginary unit. σ is set to 0 and μ_r set to 1 in calculations. In practice, when the absorption loss is considered into the MO materials, the diagonal elements ε in Eq. (2) are replaced by the complex permittivity $\varepsilon = \varepsilon + \varepsilon'$, where ε' represents finite losses. This introduces a complex propagation constant, which affects the propagation of RCP and LCP waves and causes energy to dissipate.

3.1. Square Air Holes with C_2 Symmetry Protection

3.1.1. Magnetic Field along the x/y Direction

We first study the modulation of the polarization singularities when the MO PhC slab possesses the C_2 symmetry. Due to the application of a magnetic field along the x/y direction to the MO PhC slab, the up-down mirror (σ_z) symmetry is broken, resulting in an asymmetry in the upward and downward

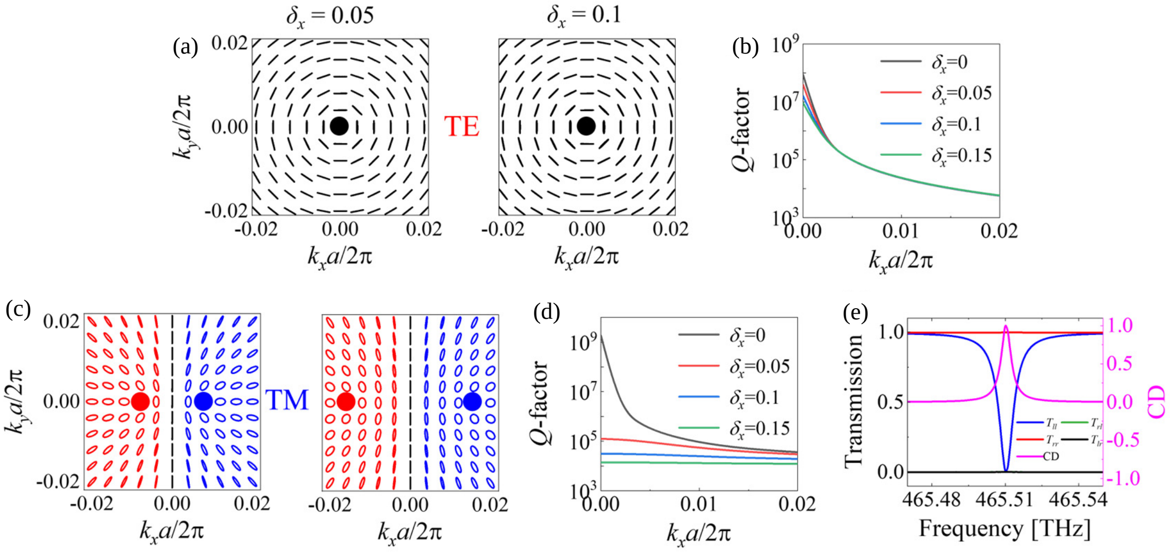

FIGURE 2. (a) Far-field polarization states of the TE band with $\delta_x = 0.05$ and $\delta_x = 0.1$. (b) Distribution of the Q-factors for the TE band at different δ_x. (c) Far-field polarization states of the TM band with $\delta_x = 0.05$ and $\delta_x = 0.1$. (d) Distribution of the Q-factors for the TM band at different δ_x. (e) Transmission and CD spectra when the TM mode has extrinsic chirality at $(k_xa/2\pi, k_ya/2\pi) = (0.008, 0)$ with $\delta_x = 0.05$.

radiation. For simplicity of analysis, we primarily investigate the far-field polarization states distribution of the upward radiation. Additionally, because the structure possesses $C_{4\text{v}}$ symmetry protection, we only analyze the effect of the magnetic field applied along the x direction on the far-field polarization states. It should be noted that the distribution of far-field polarization states under the y direction magnetic field can be obtained by rotating the distribution of far-field polarization states under the x direction magnetic field clockwise by 90 degrees. The far-field polarization states of the TE mode are unaffected by the x direction magnetic field, as shown in Figs. 2(a) and (b). A vortex and ultra-high Q-factor consistently form at the Γ point of the Brillouin zone, indicating the presence of the V point (BIC). As the strength of the x direction magnetic field increases, the Q-factor of the Γ point in the TE band shows a slight decrease.

Unlike TE mode, TM mode exhibits different characteristics under the x direction magnetic field. As shown in Fig. 2(c), the x direction magnetic field causes the V point to split into a pair of C points, with the polarization states distribution similar to that found in Fig. 1(f) when the C_2 symmetry is broken. As the magnetic field strength increases, the C+ and C− points gradually move apart. It should be noted that the location of the C point does not exhibit a mere linear variation with the increase of the δ_x due to the coupling between the TE and TM modes (see S1 in the Supplementary Material for details). The Q-factor distribution of the TM mode in Fig. 2(d) shows the evolution of the BIC at the Γ point into a QBIC under the influence of δ_x. Additionally, the Q-factor exhibits a decreasing trend as δ_x increases. Existing research has demonstrated that in-plane/out-of-plane symmetry breaking can cause the V points in both TE and TM modes to split into two C points [24]. As shown in Figs. 1(e) and (f), the results of breaking the in-plane symmetry also support this statement. The nature of MO modulation does not fundamentally alter the topological characteristics based on parameter tuning. However, considering the MO effect, the electric fields perpendicular to the applied magnetic field can result in the significant effect. The manipulation of the V point by the magnetic field along the x/y direction shows polarization sensitivity, a property that differs from the modulation method associated with structural symmetry breaking.

The emergence of the C points enables the realization of extrinsic chirality without breaking the $C_{4\text{v}}$ structural symmetry. As shown in the transmission and CD spectra in Fig. 2(e), a chiral QBIC with CD > 0.99 and a Q-factor of 67501 is achieved at $(k_xa/2\pi, k_ya/2\pi) = (0.008, 0)$ in momentum space. It should be noted that in lossy systems, the total Q-factor Q_{tot} is defined by the relation $Q_{\text{tot}}^{-1} = Q_{\text{rad}}^{-1} + Q_{\text{dis}}^{-1}$ [18, 19], where Q_{rad} and Q_{dis} are the radiative and dissipative quality factors, respectively. Consequently, Q-factor in this paper is Q_{rad}. Here, the CD is defined as the transmission difference under LCP and RCP incidence and can be expressed as [24]

$$\text{CD} = \frac{(T_{rr} + T_{lr}) - (T_{rl} + T_{ll})}{(T_{rr} + T_{lr}) + (T_{rl} + T_{ll})}, \tag{4}$$

where $T_{ij} = |t_{ij}|^2$ ($i = r, l$; $j = r, l$; r indicates RCP; l indicates LCP) represents the transmission of the output polarization i from the input polarization j. The TE and TM modes exhibit distinct modulation behaviors under the x direction magnetic field, primarily due to their different responses to Eq. (3). The TE mode and TM mode are affected differently by Eq. (3) (see S2 in the Supplementary Material for details).

3.1.2. Magnetic Field along the z Direction

When the magnetic field is applied along the z direction, the TRS of the MO PhC slab is broken whereas C_2 and σ_z symmetries are maintained, allowing the existence of SP-BIC at the Γ point. In this case, the upward and downward radiations are identical. By adjusting the direction and strength of the magnetic field, the polarization states around the V points in both

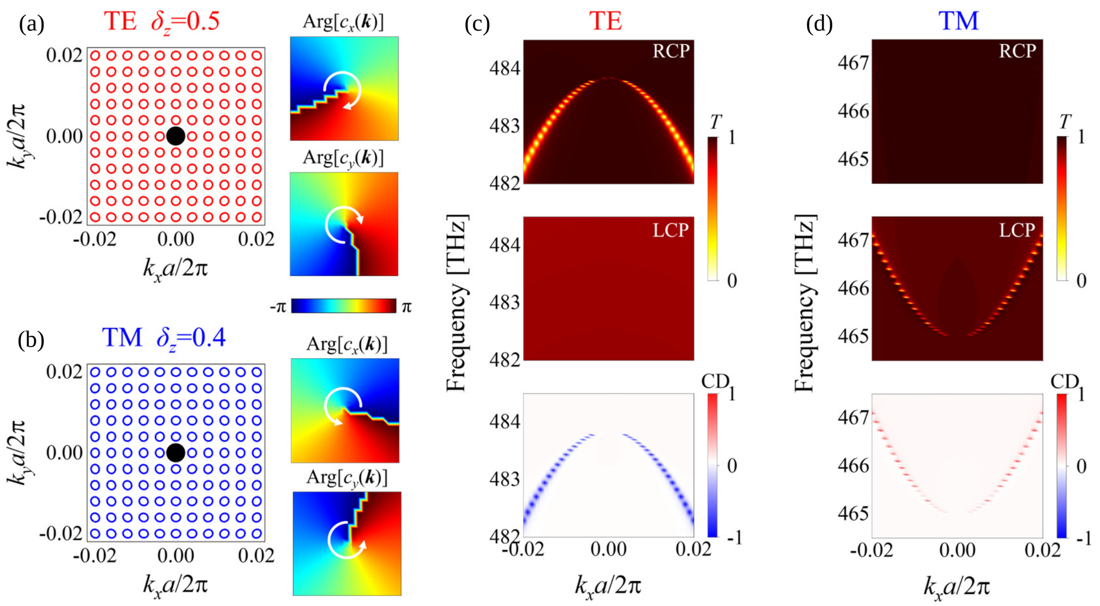

FIGURE 3. Far-field polarization states for the (a) TE band with $\delta_z = 0.5$ and the (b) TM band with $\delta_z = 0.4$. The inset shows the phase distributions of $c_x(\mathbf{k})$ and $c_y(\mathbf{k})$ in momentum space. Transmission and CD spectra of the MO PhC slab at $k_y = 0$ for the (c) TE band with $\delta_z = 0.5$ and the (d) TM band with $\delta_z = 0.4$.

TE and TM bands can be arbitrarily controlled across the entire Poincaré sphere.

Previous study has shown that only the TE mode responds to the magnetic field in the z direction in an MO PhC slab consisting of a square array of circular air holes [36]. Herein, we show that the MO PhC slab with square air holes enables the simultaneous modulation of the polarization states of both TE and TM modes. Interestingly, the far-field polarization states of the TE and TM modes exhibit opposite behaviors under the z direction magnetic modulation. As shown in Figs. 3(a) and (b), when $\delta_z = 0.5$ and $\delta_z = 0.4$, RCP and LCP states are found around the V points of TE and TM modes, respectively. The left-right handedness of the far-field polarization state can be characterized by the Stokes parameter S_3, where $S_3 > 0$ and $S_3 < 0$ correspond to the right-handed and the left-handed states, respectively. S_3 can be expressed as $S_3 = 2\text{Im}[c_x^*(\mathbf{k})c_y(\mathbf{k})]$ [7, 16, 31], where $c_x(\mathbf{k})$ and $c_y(\mathbf{k})$ denote the x and y components of the Bloch modes for the far-field polarization vector $c(\mathbf{k})$ projected onto the x-y plane, respectively. $c_x(\mathbf{k})$ and $c_y(\mathbf{k})$ can be further expressed as $c_x(\mathbf{k}) = |c_x(\mathbf{k})|e^{i\varphi(x)}$, and $c_y(\mathbf{k}) = |c_y(\mathbf{k})|e^{i\varphi(y)}$, where $\varphi(x) = \arg[c_x(\mathbf{k})]$ and $\varphi(y) = \arg[c_y(\mathbf{k})]$. Therefore, S_3 can be simplified as $S_3 = 2|c_x(\mathbf{k})|\,|c_y(\mathbf{k})|\sin(\Delta\varphi)$, with $\Delta\varphi = \arg[c_y(\mathbf{k})] - \arg[c_x(\mathbf{k})]$. Figs. 3(a) and (b) show the phase distributions of $c_x(\mathbf{k})$ and $c_y(\mathbf{k})$ for the TE mode at $\delta_z = 0.5$ and TM mode at $\delta_z = 0.4$, respectively. It can be found that the TE and TM modes exhibit phase distributions with opposite winding directions, which leads to opposite signs of S_3. Consequently, the TE and TM modes show opposite circular polarization states in the presence of δ_z.

Figure 3(c) shows the variation of transmission and CD spectra of the TE mode along k_x at $k_y = 0$. Because the momentum space is dominated by RCP states, resonances in the transmission spectra occur under RCP incidence, whereas no resonance is excited under LCP incidence, resulting in near-unity CDs (< -0.99) over a wide angular range. The CD at the Γ point is nearly zero because the eigenstate at the Γ point is BIC, which is completely decoupled from the incident wave. The TM mode exhibits the opposite trend to the TE mode. As shown in Fig. 3(d), the distribution of LCP states in momentum space leads to near-unity CDs (> 0.99) over a wide angular range. The distribution of circular polarization states in momentum space provides a new approach to achieving chiral emission over a broad range of incident angles. Under the magnetic field applied along the z direction, the evolutions of the far-field polarization states of the TE and TM modes are shown in S3 in the Supplementary Material.

3.2. Deformed Square Air Holes with Symmetry Breaking

3.2.1. Magnetic Field along the x/y Direction

The modulation of the magnetic field on C points under the in-plane C_2 symmetry breaking is studied. The structure parameters are consistent with those in Fig. 1(a), with $l_1 = 260$ nm and $\Delta l = 20$ nm. Here, we only study the far-field polarization states of the upward radiation. As shown in Fig. 4(a), when the magnetic field is applied along the x direction, the far-field polarization states of the TE mode are unaffected by the magnetic field. The C points are only influenced by breaking the C_2 symmetry. Therefore, their locations remain unchanged, same as those in Fig. 1(e), consistently located at $(k_xa/2\pi, k_ya/2\pi) = (\pm 0.012, 0)$. In contrast, the pair of C points of the TM mode gradually separates as the magnetic field strength increases. Interestingly, as shown in Fig. 4(b), when $\Delta l = 20$ nm and $\delta_x = 0.05$, the C points are located at $(k_xa/2\pi, k_ya/2\pi) = (\pm 0.016, 0)$. This phenomenon is

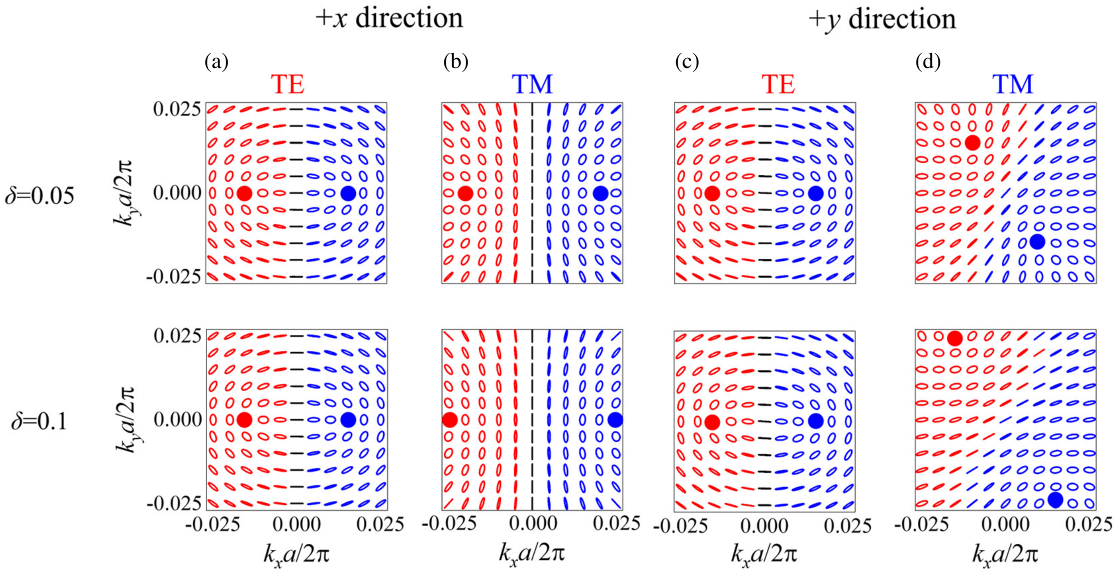

FIGURE 4. Far-field polarization states of the (a) TE and (b) TM bands under the x direction magnetic fields with different strengths. Far-field polarization states of the (c) TE and (d) TM bands under the y direction magnetic fields with different strengths.

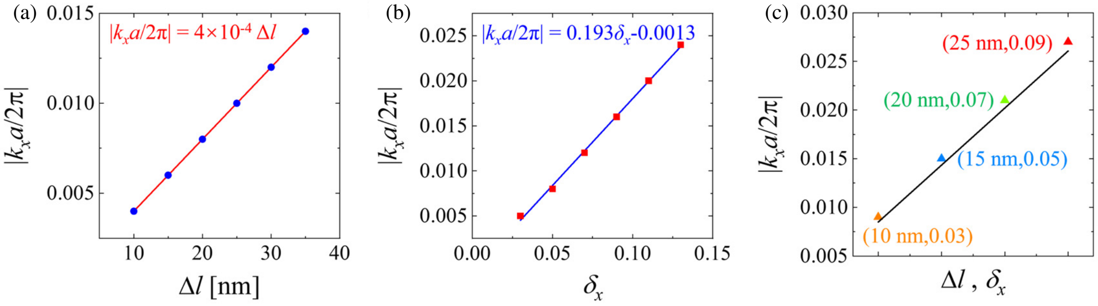

FIGURE 5. Dependence of the abscissa $|k_xa/2\pi|$ of C points in the TM mode on (a) $(\Delta l, \delta_x = 0)$, (b) $(\Delta l = 0, \delta_x)$, and (c) $(\Delta l, \delta_x)$.

due to that the C points are located at $(k_xa/2\pi, k_ya/2\pi) = (\pm 0.008, 0)$ when $\Delta l = 20\,\text{nm}$ and $\delta_x = 0$, and they are also located at $(k_xa/2\pi, k_ya/2\pi) = (\pm 0.008, 0)$ when $\Delta l = 0\,\text{nm}$ and $\delta_x = 0.05$.

Furthermore, the variations in the location of the pair of C points are investigated for the TM mode under the pure symmetry breaking $(\Delta l, \delta_x = 0)$, pure magnetic field $(\Delta l = 0, \delta_x)$, and their superposition effect $(\Delta l, \delta_x)$. As shown in Figs. 5(a) and (b), the fitted relationships under the pure symmetry breaking and the pure magnetic field are given by $|k_xa/2\pi| = 4\times 10^{-4}\Delta l$ and $|k_xa/2\pi| = 0.193\delta_x - 0.0013$, respectively. It can be found that within the presented parameter range, the location of C points increases linearly with the increase of Δl or δ_x. When considering their superposition effect, the overall fitted relationship is $|k_xa/2\pi| = 4\times 10^{-4}\Delta l + 0.193\delta_x - 0.0013$ (black line), which is in good agreement with the calculated locations of C points (dots) presented in Fig. 5(c). It can be inferred that the location Loc $(\Delta l, \delta_x)$ of the C point satisfies the relationship $\text{Loc}(\Delta l, \delta_x) \approx \text{Loc}(\Delta l, \delta_x = 0) + \text{Loc}(\Delta l = 0, \delta_x)$, indicating that the location of the C point in the TM mode is influenced by both symmetry breaking and the magnetic field.

When the magnetic field is applied along the y direction, the far-field polarization states of the TE mode remain unchanged in Fig. 4(c), and the locations of the C points stay constant — similar to the behavior observed under the x direction magnetic field. However, for the TM mode, the pair of C points no longer distributes symmetrically with respect to the $k_y = 0$ axis. Instead, they are centrally symmetric about the Γ point. As shown in Fig. 4(d), the C+ point is located at $(k_xa/2\pi, k_ya/2\pi) = (-0.01, 0.015)$ at $\delta_y = 0.05$, whereas the C− point is located at $(k_xa/2\pi, k_ya/2\pi) = (0.01, -0.015)$. The pair of C points gradually separates as the magnetic field strength increases. The modulation of C point by the magnetic field along the x/y direction exhibits polarization sensitivity similar to that of the V point.

3.2.2. Magnetic Field along the z Direction

The magnetic field applied along the z direction exhibits interesting behaviors in modulating the singularities of both TE and TM modes under the C_2 symmetry breaking. As shown in Fig. 6(a), for the TE mode, the z direction magnetic field induces changes in the relative locations of the two C points. With increasing δ_z, the C+ point gradually moves toward the

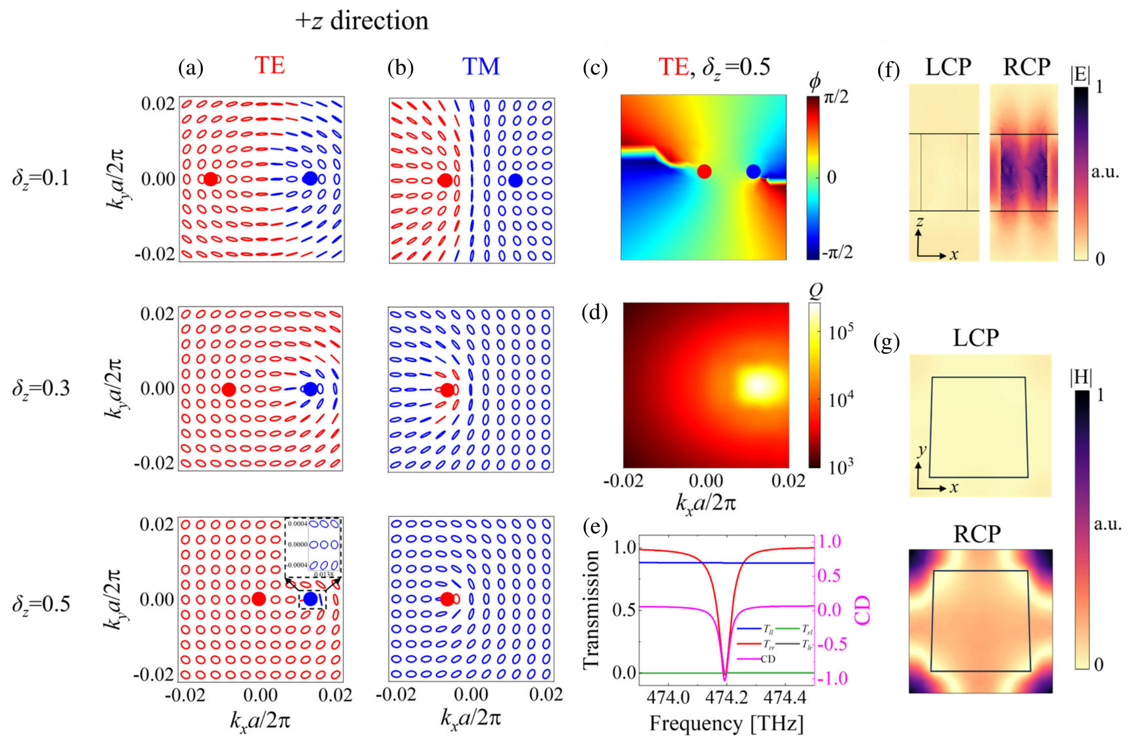

FIGURE 6. Far-field polarization states of the (a) TE and (b) TM bands under the z direction magnetic fields with different strengths. Distributions of (c) orientation angles and (d) Q-factors of the far-field polarization states for the TE mode with $\delta_z = 0.5$. (e) Transmission and CD spectra when the TE mode exhibits intrinsic chirality at Γ point with $\delta_z = 0.5$. (f) Electric and (g) magnetic near-field distributions of the MO PhC slab under LCP and RCP incidence at 474.19 THz of the TE mode extracted from the x-z and x-y plane, respectively.

Γ point, whereas the C− point remains nearly unchanged at $(k_xa/2\pi, k_ya/2\pi) = (0.0138, 0)$. As shown in Fig. 6(b), unlike the TE mode, the location of the C+ point of the TM mode remains nearly unchanged at $(k_xa/2\pi, k_ya/2\pi) = (-0.006, 0)$ when δ_z increases.

Because one of the C points in the TE mode can be moved to the Γ point by adjusting the magnetic field, this leads to the emergence of a chiral QBIC. Figs. 6(c) and (d) show the distributions of the orientation angles and Q-factors of the TE mode at $\delta_z = 0.5$, respectively. It can be found from Fig. 6(c) that the total winding orientation angle is π along a counterclockwise loop surrounding the Γ point. This indicates that the topological charge of the singularity at the Γ point is 1/2, confirming the existence of a circular polarization state. As shown in Fig. 6(d), the chiral QBIC at the Γ point has a high Q-factor of 9036. Fig. 6(e) shows the transmission and CD spectra of the TE mode under normal incidence at $\delta_z = 0.5$. Under RCP incidence, a strong resonance at 474.19 THz occurs, whereas no resonance is excited under LCP incidence. This confirms the presence of an intrinsic right-handed chiral QBIC with a near-unity CD at the Γ point. The distinct responses to LCP and RCP incidence can be represented by the distributions of electric and magnetic fields. Figs. 6(f) and (g) show the electromagnetic field distributions of the chiral QBIC in the TE mode. The chiral QBIC strongly couples with RCP incidence and strong near-field enhancement distributions can be found, whereas the chiral QBIC is decoupled from LCP incidence.

Furthermore, to better understand the resonant nature of the intrinsic chiral QBIC, the scattered powers are analyzed based on multipole decomposition (see S4 in the Supplementary Material for details). The multipole decomposition can be divided into electric dipole (ED), magnetic dipole (MD), toroidal dipole (TD), electric quadrupole (EQ), and magnetic quadrupole (MQ) modes [50, 51]. As shown in Figs. 7(a) and (b), for LCP and RCP incidence, the dominant multipole at the resonant frequency of 474.19 THz is MQ for both cases. Moreover, it is found that the MQ scattered power for RCP incidence is over three orders of magnitude greater than that for LCP incidence. This is because the eigenstate under consideration is a right-handed C point, which exhibits strong coupling with RCP incidence while decoupling from LCP incidence.

As aforementioned, the TE mode can achieve an intrinsic chiral QBIC through the combination of a single in-plane C_2 symmetry breaking and a z direction magnetic field. To realize an intrinsic chiral QBIC in the TM mode under magnetic field modulation, a single out-of-plane symmetry breaking is introduced here. As shown in Fig. 8(a), a slant-perturbation Δd is introduced, transforming the original vertical square air holes into slanted square air holes and breaking out-of-plane symmetry. The slanted structure can be fabricated by placing the MO PhC slab on a wedged substrate and using etching technology with an ion collimator [22]. Fig. 8(b) shows the evolution of the distribution of far-field polarization states of the TM mode with geometric perturbation Δd at $\delta_x = 0.03$. By introducing a non-zero δ_x, a pair of half-charge C points distributes symmetrically on two sides of the Γ point. Furthermore, if a non-zero Δd is introduced simultaneously, the entire polarization map undergoes a change, with the pair of C points shifting to the

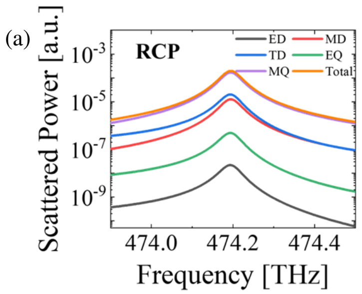

FIGURE 7. Scattered powers of different multipole moments for the chiral QBIC in the TE mode under (a) RCP and (b) LCP incidence, respectively.

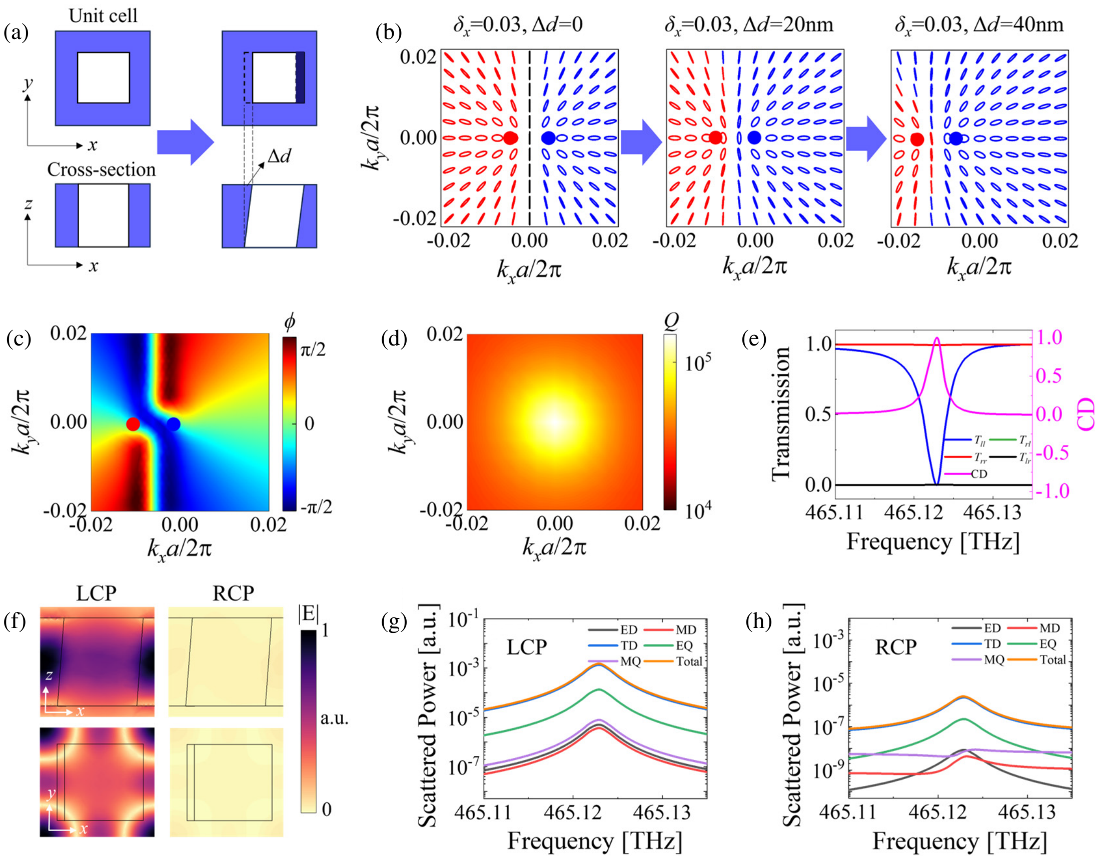

FIGURE 8. (a) Schematic of the unit cell with a slant perturbation Δd. (b) Far-field polarization states of the TM band under different Δd with $\delta_x = 0.03$. Distributions of (c) orientation angles and (d) Q-factors of the far-field polarization states for the TM band with $\delta_x = 0.03$ and $\Delta d = 20\,\text{nm}$. (e) Transmission and CD spectra when the TM mode exhibits intrinsic chirality at Γ point with $\delta_x = 0.03$ and $\Delta d = 20\,\text{nm}$. (f) Electric near-field distributions of the MO PhC slab under LCP and RCP incidence at 465.123 THz of the TM mode Scattered powers of different multipole moments for the chiral QBIC in the TM mode under (g) LCP and (h) RCP incidence, respectively.

left. When δ_x and Δd are properly combined (e.g., $\delta_x = 0.03$ and $\Delta d = 20\,\text{nm}$), the C$-$ point can be precisely located at the Γ point, thereby realizing an intrinsic chiral QBIC. If Δd is further increased, the pair of C points continues to shift to the left.

Figures 8(c) and (d) show the distributions of the orientation angles and Q-factors of the TM mode at $\delta_x = 0.03$ and $\Delta d = 20\,\text{nm}$, respectively. It can be found from Fig. 8(c) that the topological charge of the polarization singularity at the Γ point is 1/2. As shown in Fig. 8(d), the chiral QBIC at the Γ point has an ultra-high Q-factor of 154000. Based on the assumption of no losses, we obtain a chiral QBIC with an ultra-high Q-factor in the TM mode. However, when considering the absorption losses ε' in actual MO materials, the Q-factor is significantly affected. When $\varepsilon' = 0.001$, the calculated Q-factor is 5460; when $\varepsilon' = 0.005$, the Q-factor is 1124. It can be found that absorption loss leads to a rapid decrease in the Q-factor. The transmission and CD spectra of the TM mode under normal incidence at $\delta_x = 0.03$ and $\Delta d = 20\,\text{nm}$ are shown in Fig. 8(e). Under LCP incidence there is a strong resonance at 465.123 THz. However, no resonance is excited under RCP incidence. This confirms the presence of an intrinsic left-handed chiral QBIC with a near-unity CD at the Γ point. As shown in Fig. 8(f), the electric field of the chiral QBIC exhibits strong coupling with LCP incidence, whereas the field has no coupling with RCP incidence, thereby resulting in intrinsic chi-

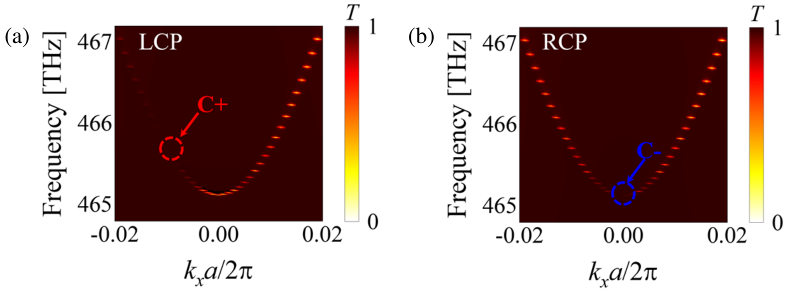

FIGURE 9. Angle-resolved transmission spectra of the MO PhC slab under (a) LCP and (b) RCP incidence.

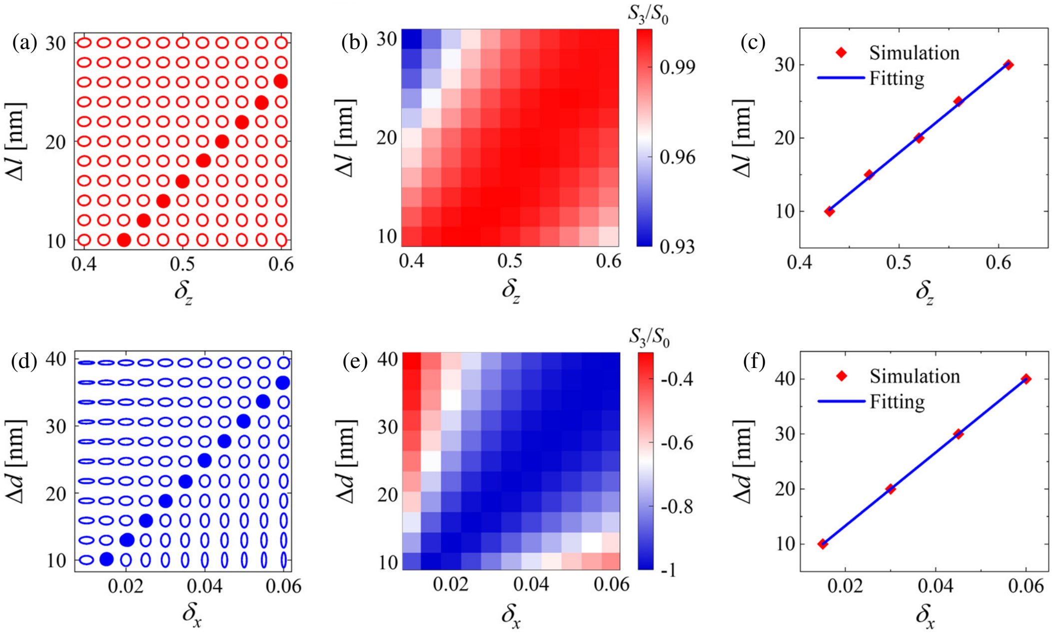

FIGURE 10. (a) Far-field polarization states and (b) normalized Stokes parameter S_3/S_0 of the TE mode as a function of δ_z and Δl at the Γ point. (c) Relationship between Δl and δ_z when the Γ point exhibits intrinsic chirality for the TE band. (d) Far-field polarization states and (e) normalized Stokes parameter S_3/S_0 of the TM mode as a function of δ_x and Δd at the Γ point. (f) Relationship between Δd and δ_x when the Γ point exhibits intrinsic chirality for the TM band.

rality. Figs. 8(g) and (h) show the multipole decomposition of the scattered powers at the resonant QBIC states. The dominant multipole at the resonant frequency of 465.123 THz is TD for LCP and RCP incidence. The MQ scattered power for LCP incidence is over three orders of magnitude greater than that for RCP incidence, indicating strong coupling with LCP incidence and decoupling from RCP incidence. Furthermore, the angle-resolved transmission spectra of a slant-perturbation MO PhC slab ($\delta_x = 0.03$, $\Delta d = 20\,\text{nm}$) under RCP and LCP incidence are calculated, as shown in Figs. 9(a) and (b). It can be found that the TM mode is excited at the Γ point under LCP incidence, and the C+ point is identified at $k_x a/2\pi = -0.01$. In contrast, under RCP incidence, the C− point represented by a vanishing point in the TM mode appears at the Γ point.

In addition, we investigate the modulation of far-field polarization states and normalized Stokes parameter S_3/S_0 by the combination of geometric perturbation and an external magnetic field at the Γ point. As shown in Figs. 10(a) and (b), for the TE mode, a series of RCP states with $S_3/S_0 > 0.99$ are generated by tuning (Δl, δ_z). The region with $S_3/S_0 = +1$ in Fig. 10(b) indicates that the C point corresponds to a pure RCP state (C+). The relationship between geometric perturbation and magnetic field magnitude for maximizing the CD of TE mode is studied when intrinsic chirality is realized. As shown in Fig. 10(c), the condition for CD maximization for the TE mode is $\Delta l/\delta_z = 100\,\text{nm}$. For the TM mode, tuning (Δd, δ_x) can generate a series of LCP states with $S_3/S_0 < -0.99$, as shown in Fig. 10(d). The region with $S_3/S_0 = -1$ in Fig. 10(e) indicates that the C point corresponds to a pure LCP state (C−). As shown in Fig. 10(f), the condition for maximum CD for the TM mode is $\Delta d/\delta_x = 621\,\text{nm}$. This provides a straightforward strategy for choosing proper combinations of $\Delta l(\Delta d)$ and $\delta_z(\delta_x)$ to achieve TE (TM) intrinsic chiral QBICs. By cooperatively reducing $\Delta l(\Delta d)$ and $\delta_z(\delta_x)$, the Q-factor of TE (TM) chiral BIC can be continuously enhanced with a near-unity CD. It should be noted that the chiral characteristics are reversed when the magnetic field is reversed (see S3 and S5 in the Supplementary Material for details). Consequently, flexible manipulation of polarization singularities in the MO PhC slab can be achieved by adjusting the magnitude and direction of the external magnetic field.

Relevant studies have shown that geometric reconfiguration enables flexible distribution of C points in momentum space by modifying the parameters of complex structures [52, 53]. However, such singularities modulation is typically one-time and irreversible. In contrast, MO modulation shows dynamic and reversible control of polarization singularities by tuning the magnetic field. Nevertheless, C point manipulation freedom appears limited in our MO modulation research, with manipulation trajectories mostly confined to a single axis. This is mainly because, under the action of a single axial magnetic field, the manipulation trajectory of C points in the MO PhC slab is strongly restricted by the direction of the magnetic field. In fact, if the magnetic field is applied no longer along a single axis, more non-zero off-diagonal elements are introduced into the permittivity tensor of the MO PhC slab, which leads to flexible motion trajectories of C points in momentum space (see S6 in the Supplementary Material for details).

4. CONCLUSIONS

We investigate the dynamic modulation of topological polarization singularities in the MO PhC slab under magnetic fields with varying directions and strengths. The magnetic fields applied along different directions (x, y, z) can effectively modulate the topological singularities of TE and TM modes. The far-field polarization states of the TE mode remain unaffected by in-plane (x/y) magnetic fields. However, the V point of the TM mode splits into two C points that separate with increasing field strength under $x(y)$-direction fields, thereby enabling extrinsic chirality without breaking C_2 symmetry. Under the z direction magnetic field, circular polarization distributions at off-Γ points are achieved for TE and TM modes, leading to near-unity CDs over a broad angular range.

Furthermore, by introducing in-plane C_2 symmetry breaking, one C point of the TE mode can be moved to the Γ point under the z direction magnetic field, resulting in an intrinsic chiral QBIC. For the TM mode, an intrinsic chiral QBIC can be achieved by combining out-of-plane symmetry breaking with magnetic field tunning. We find that the conditions for maximum CD follow $\Delta l/\delta_z = 100\,\text{nm}$ for the TE mode and $\Delta d/\delta_x = 621\,\text{nm}$ for the TM mode. The conditions provide a straightforward strategy to enhance Q-factors of chiral QBICs with near-unity CDs by simultaneously reducing geometric perturbation and field strength. This study provides flexible engineering of topological polarization singularities in momentum space in the MO PhC slab, significantly broadening the application of topological photonics in light-matter interactions.

ACKNOWLEDGEMENT

This work was supported by the National Natural Science Foundation of China (Grant Nos. 62275243, 62075209, and 61675193).

REFERENCES

[1] Berry, M. V., "The singularities of light: Intensity, phase, polarisation," *Light: Science & Applications*, Vol. 12, No. 1, 238, 2023.

[2] Liu, W., W. Liu, L. Shi, and Y. Kivshar, "Topological polarization singularities in metaphotonics," *Nanophotonics*, Vol. 10, No. 5, 1469–1486, 2021.

[3] Wang, F., X. Yin, Z. Zhang, Z. Chen, H. Wang, P. Li, Y. Hu, X. Zhou, and C. Peng, "Fundamentals and applications of topological polarization singularities," *Frontiers in Physics*, Vol. 10, 862962, 2022.

[4] Hsu, C. W., B. Zhen, A. D. Stone, J. D. Joannopoulos, and M. Soljačić, "Bound states in the continuum," *Nature Reviews Materials*, Vol. 1, No. 9, 16048, 2016.

[5] Zhen, B., C. W. Hsu, L. Lu, A. D. Stone, and M. Soljačić, "Topological nature of optical bound states in the continuum," *Physical Review Letters*, Vol. 113, No. 25, 257401, 2014.

[6] Liu, W., B. Wang, Y. Zhang, J. Wang, M. Zhao, F. Guan, X. Liu, L. Shi, and J. Zi, "Circularly polarized states spawning from bound states in the continuum," *Physical Review Letters*, Vol. 123, No. 11, 116104, 2019.

[7] Zeng, Y., G. Hu, K. Liu, Z. Tang, and C.-W. Qiu, "Dynamics of topological polarization singularity in momentum space," *Physical Review Letters*, Vol. 127, No. 17, 176101, 2021.

[8] Yin, X., J. Jin, M. Soljačić, C. Peng, and B. Zhen, "Observation of topologically enabled unidirectional guided resonances," *Nature*, Vol. 580, No. 7804, 467–471, 2020.

[9] Yin, X., T. Inoue, C. Peng, and S. Noda, "Topological unidirectional guided resonances emerged from interband coupling," *Physical Review Letters*, Vol. 130, No. 5, 056401, 2023.

[10] Ni, X., Y. Liu, B. Lou, M. Zhang, E. L. Hu, S. Fan, E. Mazur, and H. Tang, "Three-dimensional reconfigurable optical singularities in bilayer photonic crystals," *Physical Review Letters*, Vol. 132, No. 7, 073804, 2024.

[11] Zheng, B. J., W. J. Shi, H. Y. Dong, Y. T. Li, J. Q. Li, Z.-G. Dong, and J. Wang, "Dynamical control of topological unidirectional guided resonances via external magnetic field," *Physical Review Research*, Vol. 7, No. 1, 013091, 2025.

[12] Huang, L. and A. E. Miroshnichenko, "Evolution of topological polarization singularity in a photonic crystal slab," *Laser & Photonics Reviews*, Vol. 19, No. 18, e00555, 2025.

[13] Kang, M., S. Zhang, M. Xiao, and H. Xu, "Merging bound states in the continuum at off-high symmetry points," *Physical Review Letters*, Vol. 126, No. 11, 117402, 2021.

[14] Jin, J., X. Yin, L. Ni, M. Soljačić, B. Zhen, and C. Peng, "Topologically enabled ultrahigh-Q guided resonances robust to out-of-plane scattering," *Nature*, Vol. 574, No. 7779, 501–504, 2019.

[15] Kang, M., L. Mao, S. Zhang, M. Xiao, H. Xu, and C. T. Chan, "Merging bound states in the continuum by harnessing higher-order topological charges," *Light: Science & Applications*, Vol. 11, No. 1, 228, 2022.

[16] Ye, W., Y. Gao, and J. Liu, "Singular points of polarizations in the momentum space of photonic crystal slabs," *Physical Review Letters*, Vol. 124, No. 15, 153904, 2020.

[17] Chen, Z., X. Yin, J. Jin, Z. Zheng, Z. Zhang, F. Wang, L. He, B. Zhen, and C. Peng, "Observation of miniaturized bound states in the continuum with ultra-high quality factors," *Science Bulletin*, Vol. 67, No. 4, 359–366, 2022.

[18] Liang, Y., K. Koshelev, F. Zhang, H. Lin, S. Lin, J. Wu, B. Jia, and Y. Kivshar, "Bound states in the continuum in anisotropic plasmonic metasurfaces," *Nano Letters*, Vol. 20, No. 9, 6351–6356, 2020.

[19] Liang, Y., D. P. Tsai, and Y. Kivshar, "From local to nonlocal high-Q plasmonic metasurfaces," *Physical Review Letters*, Vol. 133, No. 5, 053801, 2024.

[20] Doeleman, H. M., F. Monticone, W. den Hollander, A. Alù, and A. F. Koenderink, "Experimental observation of a polarization

vortex at an optical bound state in the continuum," *Nature Photonics*, Vol. 12, No. 7, 397–401, 2018.

[21] Hsu, C. W., B. Zhen, J. Lee, S.-L. Chua, S. G. Johnson, J. D. Joannopoulos, and M. Soljačić, "Observation of trapped light within the radiation continuum," *Nature*, Vol. 499, No. 7457, 188–191, 2013.

[22] Gorkunov, M. V., A. A. Antonov, and Y. S. Kivshar, "Metasurfaces with maximum chirality empowered by bound states in the continuum," *Physical Review Letters*, Vol. 125, No. 9, 093903, 2020.

[23] Shi, T., Z.-L. Deng, G. Geng, X. Zeng, Y. Zeng, G. Hu, A. Overvig, J. Li, C.-W. Qiu, A. Alù, Y. S. Kivshar, and X. Li, "Planar chiral metasurfaces with maximal and tunable chiroptical response driven by bound states in the continuum," *Nature Communications*, Vol. 13, No. 1, 4111, 2022.

[24] Chen, Y., H. Deng, X. Sha, W. Chen, R. Wang, Y.-H. Chen, D. Wu, J. Chu, Y. S. Kivshar, S. Xiao, and C.-W. Qiu, "Observation of intrinsic chiral bound states in the continuum," *Nature*, Vol. 613, No. 7944, 474–478, 2023.

[25] Kodigala, A., T. Lepetit, Q. Gu, B. Bahari, Y. Fainman, and B. Kanté, "Lasing action from photonic bound states in continuum," *Nature*, Vol. 541, No. 7636, 196–199, 2017.

[26] Huang, C., C. Zhang, S. Xiao, Y. Wang, Y. Fan, Y. Liu, N. Zhang, G. Qu, H. Ji, J. Han, *et al.*, "Ultrafast control of vortex microlasers," *Science*, Vol. 367, No. 6481, 1018–1021, 2020.

[27] Ha, S. T., Y. H. Fu, N. K. Emani, Z. Pan, R. M. Bakker, R. Paniagua-Domínguez, and A. I. Kuznetsov, "Directional lasing in resonant semiconductor nanoantenna arrays," *Nature Nanotechnology*, Vol. 13, No. 11, 1042–1047, 2018.

[28] Chen, A., W. Liu, Y. Zhang, B. Wang, X. Liu, L. Shi, L. Lu, and J. Zi, "Observing vortex polarization singularities at optical band degeneracies," *Physical Review B*, Vol. 99, No. 18, 180101, 2019.

[29] Liu, Z., Y. Xu, Y. Lin, J. Xiang, T. Feng, Q. Cao, J. Li, S. Lan, and J. Liu, "High-Q quasibound states in the continuum for nonlinear metasurfaces," *Physical Review Letters*, Vol. 123, No. 25, 253901, 2019.

[30] Wang, B., W. Liu, M. Zhao, J. Wang, Y. Zhang, A. Chen, F. Guan, X. Liu, L. Shi, and J. Zi, "Generating optical vortex beams by momentum-space polarization vortices centred at bound states in the continuum," *Nature Photonics*, Vol. 14, No. 10, 623–628, 2020.

[31] Yoda, T. and M. Notomi, "Generation and annihilation of topologically protected bound states in the continuum and circularly polarized states by symmetry breaking," *Physical Review Letters*, Vol. 125, No. 5, 053902, 2020.

[32] Zhou, H., X. Ni, B. Lou, S. Fan, Y. Cao, and H. Tang, "Control of chirality and directionality of nonlinear metasurface light source via moiré engineering," *Physical Review Letters*, Vol. 134, No. 4, 043801, 2025.

[33] He, H., L. Wang, H. Duan, X. Yan, Y. Zhang, S. Luo, Y. Yi, and C. Zhou, "Topological polarization singularity modulation in the phase change material metasurfaces," *IEEE Photonics Technology Letters*, Vol. 37, No. 14, 805–808, 2025.

[34] Yao, E., Z. Su, Y. Bi, Y. Wang, and L. Huang, "Tunable quasi-bound states in the continuum in magneto-optical metasurfaces," *Journal of Physics D: Applied Physics*, Vol. 57, No. 37, 375104, 2024.

[35] Lv, W., H. Qin, Z. Su, C. Zhang, J. Huang, Y. Shi, B. Li, P. Genevet, and Q. Song, "Robust generation of intrinsic C points with magneto-optical bound states in the continuum," *Science Advances*, Vol. 10, No. 46, eads0157, 2024.

[36] Tu, Q.-A., H. Zhou, D. Zhao, Y. Meng, M. Gong, and Z. Gao, "Magnetically tunable bound states in the continuum with arbitrary polarization and intrinsic chirality," *Photonics Research*, Vol. 12, No. 12, 2972–2982, 2024.

[37] Zhao, C., S. Dong, Q. Zhang, Y. Zeng, G. Hu, and Y. Zhang, "Magnetic modulation of topological polarization singularities in momentum space," *Optics Letters*, Vol. 47, No. 11, 2754–2757, 2022.

[38] Zhao, X., J. Wang, W. Liu, Z. Che, X. Wang, C. T. Chan, L. Shi, and J. Zi, "Spin-orbit-locking chiral bound states in the continuum," *Physical Review Letters*, Vol. 133, No. 3, 036201, 2024.

[39] Yang, B., W. Zheng, and A. Liu, "Magnetically tunable ultrahigh Q-factor intrinsic chirality based on merging bound states in the continuum," *Optics Express*, Vol. 33, No. 16, 34 960–34 973, 2025.

[40] Zhang, Y., A. Chen, W. Liu, C. W. Hsu, B. Wang, F. Guan, X. Liu, L. Shi, L. Lu, and J. Zi, "Observation of polarization vortices in momentum space," *Physical Review Letters*, Vol. 120, No. 18, 186103, 2018.

[41] Wu, J., J. Chen, X. Qi, Z. Guo, J. Wang, F. Wu, Y. Sun, Y. Li, H. Jiang, L. Shi, J. Zi, and H. Chen, "Observation of accurately designed bound states in the continuum in momentum space," *Photonics Research*, Vol. 12, No. 4, 638–647, 2024.

[42] Haider, T., "A review of magneto-optic effects and its application," *International Journal of Electromagnetics and Applications*, Vol. 7, No. 1, 17–24, 2017.

[43] Buschow, K. H. J., *Handbook of Magnetic Materials*, Elsevier, 2003.

[44] Jesenska, E., T. Yoshida, K. Shinozaki, T. Ishibashi, L. Beran, M. Zahradnik, R. Antos, M. Kučera, and M. Veis, "Optical and magneto-optical properties of Bi substituted yttrium iron garnets prepared by metal organic decomposition," *Optical Materials Express*, Vol. 6, No. 6, 1986–1997, 2016.

[45] Rizal, C., H. Shimizu, and J. R. Mejía-Salazar, "Magneto-optics effects: New trends and future prospects for technological developments," *Magnetochemistry*, Vol. 8, No. 9, 94, 2022.

[46] Yang, W., Q. Liu, H. Wang, Y. Chen, R. Yang, S. Xia, Y. Luo, L. Deng, J. Qin, H. Duan, and L. Bi, "Observation of optical gyromagnetic properties in a magneto-plasmonic metamaterial," *Nature Communications*, Vol. 13, No. 1, 1719, 2022.

[47] Wang, Z. and S. Fan, "Magneto-optical defects in two-dimensional photonic crystals," *Applied Physics B*, Vol. 81, No. 2, 369–375, 2005.

[48] Zhang, K. and D. Li, *Electromagnetic Theory for Microwaves and Optoelectronics*, Springer, 1998.

[49] Li, J., Z. Wu, D. Zhang, Y. Sun, W. Liu, and T. Yu, "Nonreciprocal toroidal dipole resonance and one-way quasi-bound state in the continuum," *Optics Letters*, Vol. 49, No. 5, 1313–1316, 2024.

[50] Li, M., G. Hu, X. Chen, C.-W. Qiu, H. Chen, and Z. Wang, "Topologically reconfigurable magnetic polaritons," *Science Advances*, Vol. 8, No. 50, eadd6660, 2022.

[51] Li, S., C. Zhou, T. Liu, and S. Xiao, "Symmetry-protected bound states in the continuum supported by all-dielectric metasurfaces," *Physical Review A*, Vol. 100, No. 6, 063803, 2019.

[52] Zhao, W. K., S. Y. Wang, Y. H. Jing, H. Ge, Q. Wang, Y. Q. Zeng, B. W. Jia, and N. Xu, "Giant structurally modulated intrinsic chirality of quasi-bound states in continuum," *Optics Letters*, Vol. 50, No. 5, 1649–1652, 2025.

[53] Zhang, Y., Q. Song, B. Hou, and Z. Yi, "Steerable intrinsic chirality mediated by toroidal dipole bound states in the continuum in an active metasurface," *Optics Letters*, Vol. 50, No. 9, 2868–2871, 2025.